PROCEEDINGS, 46th Workshop on Geothermal Reservoir Engineering
Stanford University, Stanford, California, February 15-17, 2021
SGP-TR-218

Modeling the Dynamic Flow Resistance Across the Fracture Network of EGS Collab Experiment 1

M.D. White[1], J.A. Burghardt[2], and EGS Collab Team[3]

[1]Energy and Environment Directorate, Pacific Northwest National Laboratory, Richland, WA 99352, USA

[1]mark.white@pnnl.gov, [2]jeffrey.burghardt@pnnl.gov

Keywords: Numerical Simulation, Embedded Fractures and Boreholes, EGS Collab, Meso-Scale EGS Experiment, Sanford Underground Research Facility, Thermal Recovery, Dynamic Fracture Aperture

ABSTRACT

EGS Collab is a series of meso-scale experiments and associated numerical simulation activities being funded by the United States Department of Energy, Geothermal Technologies Office (GTO) to investigate enhanced geothermal system processes under in-situ stress and slightly elevated temperature conditions. This project is designed to provide scientists and engineers with immediate access to impermeable rock under large compressive stresses at scales larger than possible in the laboratory, but generally smaller than those for commercial production. Immediate access to rock is provided via the existing drifts of the former Homestake Gold Mine, now operated as the Sanford Underground Research Facility in Lead, South Dakota. Experiment 1 involved the creation of a fracture network hydraulically connecting two boreholes within a volume of predominately phyllite of the Precambrian Poorman formation off the western side of the West Access drift on the 4850 Level, at approximately 1500 mbgs. The second stage of the experiment involved the injection of chilled water (i.e., around 11˚C) into hydraulic fractures created during the stimulation stage via a packed interval around 50 m from the borehole collar at the drift rib, over a period of 196 days. Flow rates and temperatures of Experiment 1 were significantly lower than those anticipated for commercial EGS reservoirs, however, one of the objectives of the EGS Collab project is to investigate and understand the fundamental processes observed during the experiment, and to translate those learnings into numerical simulators that can then be extended to commercial-scale EGS. An immediate beneficiary of these analyses is the EGS reservoir being developed for the Frontier Observatory for Research in Geothermal Energy (FORGE), the GTO's flagship EGS research effort. This paper is focused on understanding the dynamic nature of the flow resistance across the fracture network of EGS Collab Experiment 1. The fracture network of Experiment 1 included hydraulic fractures induced from the stimulation borehole, natural fractures, weep zones, splay hydraulic fractures, and damaged, but grouted monitoring boreholes. The production borehole was intersected via a hydraulically active natural fracture and the dominate hydraulic fracture. Over the course of the chilled-water injection test, the injection rate and temperature of the injected water remained nearly constant, with the exception of occasional outages, however, volumetric recoveries and network flow resistance both increased in a nominally steady fashion over time. More interestingly the network flow resistance dropped sharply with injection pumping halts, regardless of the halt duration, followed by rapid recovery of the injection pressure. The embedded borehole and fracture modeling approach couples flow and transport in the rock matrix, boreholes and fractures via three distinct but analogous discretizations. This approach was successful in modeling the seemingly disparate rapid tracer and delayed thermal recoveries of Experiment 1. For this study, the embedded borehole and fracture modeling approach is coupled with geomechanics (i.e., thermal-hydraulic-mechanical (THM) coupling) to investigate the dynamic behavior of the fracture aperture and thus flow resistance in response to changes in matrix rock temperature and pore pressure for EGS Collab Experiment 1. The principal objective of the study is to understand the observed increased flow resistance across the fracture network, but additionally to provide some insight to observed sharp drops in flow resistance with injection pumping halts.

1. INTRODUCTION

The United States Department of Energy (DOE), Office of Energy Efficiency and Renewable Energy (EERE), Geothermal Technologies Office (GTO) has been financially and technically supporting a series of meso-scale experiments and associated numerical validation

[3] J. Ajo-Franklin, T. Baumgartner, K. Beckers, D. Blankenship, A. Bonneville, L. Boyd, S. Brown, J.A. Burghardt, C. Chai, A. Chakravarty, T. Chen, Y. Chen, B. Chi, K. Condon, P.J. Cook, D. Crandall, P.F. Dobson, T. Doe, C.A. Doughty, D. Elsworth, J. Feldman, Z. Feng, A. Foris, L.P. Frash, Z. Frone, P. Fu, K. Gao, A. Ghassemi, Y. Guglielmi, B. Haimson, A. Hawkins, J. Heise, C. Hopp, M. Horn, R.N. Horne, J. Horner, M. Hu, H. Huang, L. Huang, K.J. Im, M. Ingraham, E. Jafarov, R.S. Jayne, T.C. Johnson, S.E. Johnson, B. Johnston, S. Karra, K. Kim, D.K. King, T. Kneafsey, H. Knox, J. Knox, D. Kumar, K. Kutun, M. Lee, D. Li, J. Li, K. Li, Z. Li, M. Maceira, P. Mackey, N. Makedonska, C.J. Marone, E. Mattson, M.W. McClure, J. McLennan, T. McLing, C. Medler, R.J. Mellors, E. Metcalfe, J. Miskimins, J. Moore, C.E. Morency, J.P. Morris, T. Myers, S. Nakagawa, G. Neupane, G. Newman, A. Nieto, T. Paronish, R. Pawar, P. Petrov, B. Pietzyk, R. Podgorney, Y. Polsky, J. Pope, S. Porse, J.C. Primo, C. Reimers, B.Q. Roberts, M. Robertson, V. Rodriguez-Tribaldos, W. Roggenthen, J. Rutqvist, D. Rynders, M. Schoenball, P. Schwering, V. Sesetty, C.S. Sherman, A. Singh, M.M. Smith, H. Sone, E.L. Sonnenthal, F.A. Soom, D.P. Sprinkle, S. Sprinkle, C.E. Strickland, J. Su, D. Templeton, J.N. Thomle, C. Ulrich, N. Uzunlar, A. Vachaparampil, C.A. Valladao, W. Vandermeer, G. Vandine, D. Vardiman, V.R. Vermeul, J.L. Wagoner, H.F. Wang, J. Weers, N. Welch, J. White, M.D. White, P. Winterfeld, T. Wood, S. Workman, H. Wu, Y.S. Wu, E.C. Yildirim, Y. Zhang, Y.Q. Zhang, Q. Zhou, M.D. Zoback

studies, which are serving as a research and development bridge to the field-scale experiments and simulations of the newly started Frontier Observatory for Research in Geothermal Energy (FORGE) investigations (Moore, 2020, Moore *et al.*, 2020). This project, the Stimulation Investigations for Geothermal Modeling Analysis and Validation, termed EGS Collab, is being led by the Lawrence Berkeley National Laboratory (LBNL), but is a highly collaborative venture involving seven U.S. National Laboratories, universities, and private industry (Dobson *et al.*, 2017, Kneafsey *et al.*, 2018, Kneafsey *et al.*, 2019). Principal objectives of the EGS Collab project are to develop experimental testbeds with normal- and shear-opening fracture networks between hydraulically connected boreholes under representative EGS stress conditions, but low temperature conditions, and then to compare numerical simulation forecasts against the experimental observations. Numerical simulations over the course of the project have been applied to guide experiment design, forecast fracture network initiation, development and extension, and validate the use of conservative and partitioning tracer recovery as an analog for thermal recovery and reservoir performance.

EGS Collab has completed the experimental elements of Experiment 1, which was conducted within a volume of predominately phyllite rock on the western side of the 4850 Level West Access Drift (drift) within Sanford Underground Research Facility (SURF) near the kISMET site (Oldenburg *et al.*, 2016). This experiment involved two stages: 1) stimulation - the creation of a hydraulic fracture from a sub-horizontal borehole drilled nominally in the direction of the principal minimum horizontal stress (i.e., S_{hmin}); and 2) circulation – the circulation of fluids between an injection well and one or more production wells intersecting the created fracture. At this writing, a series of eight boreholes have been drilled from the drift: 1) injection [E1-I], 2) production [E1-P], 3) two fracture orthogonal monitoring [E1-OT, E1-OB], 4) two deep fracture parallel monitoring [E1-PDT, E1-PDB], and 5) two shallow fracture parallel monitoring [E1-PST, E1-PSB]. Indications from the kISMET project were that S_{hmin} was nearly horizontal, but for the ease of conveyance and grouting all boreholes plunged downward with the injection and production boreholes were drilled with a 356° trend and 12° plunge. The two fracture orthogonal monitoring wells were drilled with the same azimuth of S_{hmin}, (i.e., with a 356° trend), but at higher and lower plunges, forming a vertical "v" shape with the apex at the drift wall. The two fracture parallel monitoring wells were drilled orthogonal to the injection and production boreholes, forming a 12° tilled "v" shape with the apex at the drift wall. Corrected S_{hmin} directions from the kISMET borehole stress measurements are a 2˚ trend with a 9.3˚ plunge (Dobson *et al.*, 2020).

Four stimulation tests, a short-term and intermediate-term ambient-fluid circulation tests, and a long-term chilled-water circulation test were completed in the Experiment 1 Test Bed (E1TB) (Kneafsey *et al.*, 2020). The long-term chilled water circulation test was executed via hydraulic fractures created near the 164' Notch (i.e., 50 m from the borehole collar) in the E1-I borehole that intersected a natural fracture, referred to as the OT-P connector, and the E1-P borehole. The OT-P fracture also intersected the E1-P borehole, yielding at least two hydraulic pathways between the E1-I and E1-P borehole. The first connection is directly from the E1-I borehole through the hydraulic fracture, intersecting the E1-P borehole below the packed interval. The second connection is through the hydraulic fracture, then along the OT-P connector, intersecting E1-P borehole within the packed interval. The long-term chilled-water circulation test was started on May 8, 2019 (10:15 MDT, 17:15 UTC) and continued for 196 days. Except for occasional outages chilled water was injected at a constant rate of 0.4 L/min, a rate that did not result in additional micro-seismicity, indicating a stable hydraulic fracture extent. Throughout this experiment a straddle packer was located over the intersection of the OT-P Connector fracture and E1-P at a depth of 121.75 ft (37.1 m) from the borehole collar, allowing for the recovery of water from the region with the straddle packer interval (E1-PI) and below the interval (E1-PB), where the hydraulic fracture intersects the E1-P borehole. Water recovery was recorded during the chilled water experiment via flow meters from the packed-off interval in E1-P (denoted E1-PI), E1-P below the packed-off interval (denoted E1-PB), E1-PST, E1-PSB, E1-PDT, E1-PDB, E1-OT, E1-OB, from below the packed-off interval in E1-I (denoted E1-IB) , from the collar of E1-I (denoted E1-IC), and manually from the weep zone (noted as the Shallow Fracture Zone) at the drift rib, using a water collection ledge carved into the drift rib on April 26, 2109. Water flows from all of the metered locations were noted throughout the course of the chilled water experiment, but near the end of the experiment water production was predominately from E1-PB and E1-PI, with small amounts from E1-PST and E1-PDT. Volumetric recovery of the injected water approached 98% near the end of the experiment.

The long-term chilled water experiment yield three scientifically interesting responses: 1) nearly instantaneous drop in injection pressure when injection switched from ambient temperature water to chilled water, 2) sharp drop in injection pressure following an injection halt, and 3) a steady gradual increase in flow resistance across the fracture network over time. The test was originally planned to be preceded with an injection period of water at ambient temperature (i.e., unchilled). Reopening pressure for the hydraulic fracture was not anticipated to be slightly higher than the minimum horizontal stress (21.7 MPa (3147 psi)), but as shown in time period "a" in Figure 1, the injection pressure at an injection rate of 0.4 L/min increased from 30.83 MPa (4472 psi) to 31.61 MPa (4585 psi), before injecting chilled water. With the injection of chilled water, shown as the end of period "a" in Figure 1, the E1-I interval pressure dropped to 29.51 MPa (4280 psi), nearly instantaneously. The injection-water chillers remained on throughout the remainder of the long-term chilled-water test, except for short periods of time for operational issues (e.g., chiller maintenance, injection tank cleaning, power outage). During each of these types of events, noted as "b", "c", and "d" in Figure 1, there was an associated increase in the injection pressure with an increase in the temperature of the injection water. This observation suggest a near borehole thermo-geomechanical process controlling the flow resistance. This could be modelled as a temperature-dependent wellbore skin factor, but that approach does not provide any insight to the mechanism behind the observation. The steady increase in injection pressure or flow resistance over the course of the long-term, chilled-water circulation test, as seen in Figure 1, for a constant rate of injected water and nearly constant injection temperature, is the focus of this study. The hypothesis to be tested is whether water leaking from the fracture surfaces into the rock matrix yields increased normal stresses on the fracture and reduced fracture aperture. To test this hypothesis the fracture network developed to investigate tracer and heat recovery during the long-term, chilled-water circulation test (White *et al.*, 2020) was modified such that the fracture aperture of the hydraulic fracture was dynamic (i.e., dependent on net pressure, the difference between fluid pressure and normal stress). Development of a mathematical model for this dependence is described in the following section.

2. FRACTURE APERTURE MODEL

The embedded fracture and borehole modeling approach (White *et al.*, 2020) was implemented into STOMP-GT, a finite-volumed based multiphase flow and transport simulator, originally designed to model the performance of radioactive waste repositories in subsurface environments, such as Yucca Mountain, and recently applied during the GTO code comparison study (White *et al.*, 2018). Spatial discretization is via hexahedral grids, and a porothermoelastic geomechanics solver is implemented in the simulator, allowing for sequential coupling of flow and transport and geomechanics. The geomechanics solver is finite-element based, using the same hexahedron grid structure for the elements. Embedded fractures and boreholes, however, are not considered in the geomechanics system of STOMP-GT. Prior to implementing a modeling approach to account for rock deformation of fractured systems, such as the displacement-discontinuity method, for which a recent simplified approach has been developed for vertically oriented fractures (Wu & Olson, 2015), a alternative model was sought. The conceptual fracture network developed for this study involved one hydraulic and one natural fracture, oriented nearly vertical. The hydraulic fracture intersected the natural fracture near the E1-P borehole. The hydraulic fracture was considered to have a stress dependent aperture, whereas the natural fracture had a fixed fracture aperture. Four assumptions were made in developing a local stress-dependent aperture model for the hydraulic fracture.

1. Local changes in fracture aperture were independent of remote changes in fracture aperture
2. Shear displacement dilation is ignored
3. Fracture closure and opening models could be combined to span negative and positive net pressures
4. Fracture extent was fixed, and the fluid pressures remained below the extension pressures

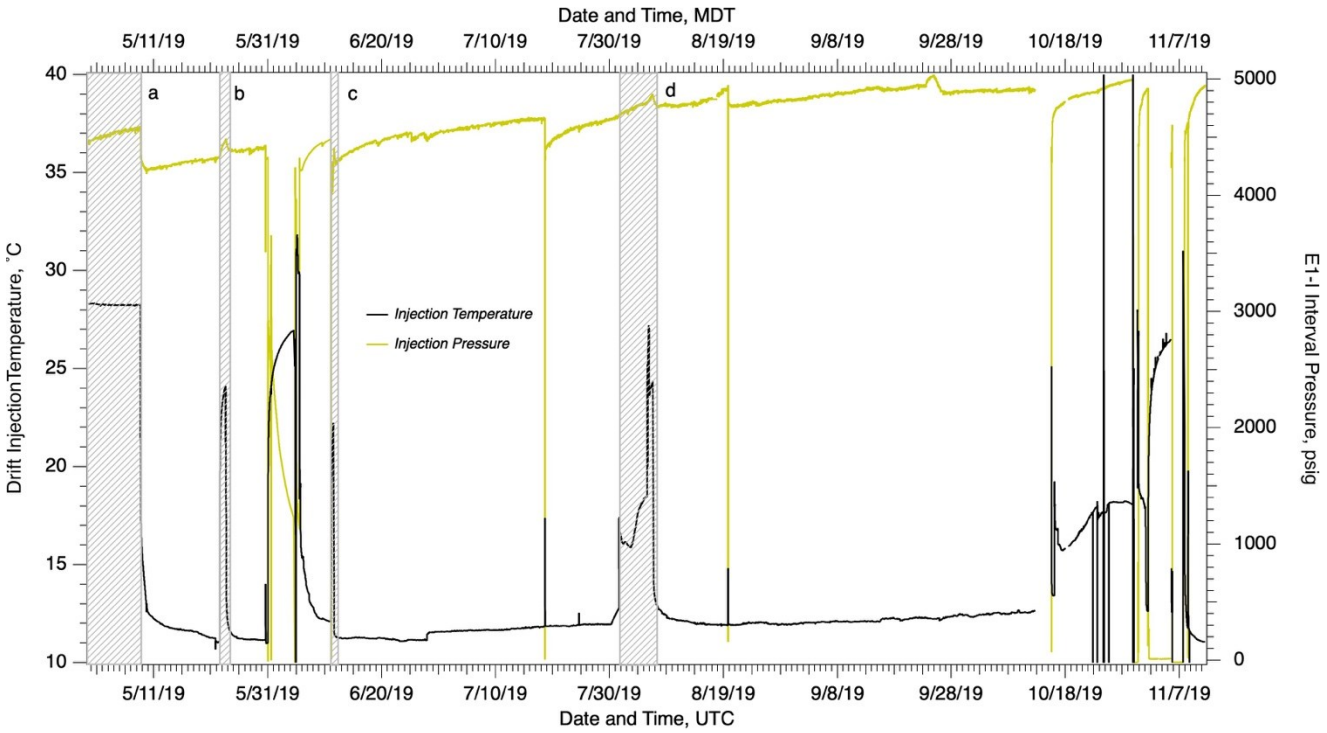

Figure 1: Temperature of water at the borehole collar and pressure within the injection interval during the long-term, chilled-water circulation test for borehole E1-I.

Normal closure can be computed by the Bandis hyperbolic model (Bandis *et al.*, 1983):

$$\delta_{nc} = \frac{k_{n0}\,(b_m)^2}{k_{n0}\,b_m + \sigma_{n\,eff}} \tag{1}$$

where δ_{nc} is the normal closure (mm), k_{n0} is the initial fracture normal stiffness (MPa/mm), b_m fracture aperture at zero normal stress (m), and $\sigma_{n\,eff}$ is the effective normal stress (MPa). This expression can be arranged in terms of fracture aperture for negative net pressure (i.e., fracture fluid pressure – normal fracture stress):

$$b_c = b_{max} - \frac{P_{net}\,b_{max}}{P_{net} - b_{max}\,k_{n0}} \tag{2}$$

where b_c is closure fracture aperture (mm), and P_{net} is the net pressure (MPa). For penny-shaped fractures the Sneddon solutions (Sneddon, 1946) for positive net pressure yield a distribution of apertures as a function of the distance from the fracture centroid and host rock geomechanical properties:

$$b_o = b_{max} + \frac{8\,(1-\upsilon^2)}{\pi\,E}\,P_{net}\,\sqrt{L^2 - r^2} \tag{3}$$

where b_o is the opening fracture aperture (mm), υ is the Poisson ratio, E is the Young's modulus (MPa), P_{net} is the net pressure, L is the overall fracture radius, and r is the distance from the fracture centroid. The net pressure is fluid pressure in the fracture minus the normal stress on the fracture correction for thermal contraction/expansion, minus the local matrix pore pressure times the Biot coefficient. To allow for more complex fracture shapes the concept was taken that the overall fracture radius and distance from the fracture centroid could varying across the fracture shape, based on finding poles of inaccessibility across the fracture shape and associated radii. A discrete number of poles were located and the overall radius and distance from the pole at a point on the fracture was determined as the average of those poles and radial extents that encompassed that point. The closure and opening fracture aperture were combined across zero net pressure, using a Sigmoid function and imposing a Sneddon radial distribution on the closure aperture:

$$b = S_f\,b_o + \left(1 - S_f\right) b_c\,\frac{\sqrt{L^2-r^2}}{L}; \quad S_f = \frac{1.0}{\left(1.0+\exp(-P_{net})\right)} \tag{4}$$

where b is the fracture aperture (mm), S_f is the Sigmoid function, which varies from 0 to 1, across the zero point of net pressure. A graphical representation of the functions in Equations 1 through 4 is shown in Figure 2 at the centroid of a fracture. The Sigmoid function provides for a numerically smooth transition from conditions of negative to positive net pressure, but there is a sharp change in variation in fracture aperture with net pressure at the zero transition point, which must be resolved by the nonlinear solvers of the STOMP-GT simulator. Fracture permeability varies over several orders of magnitude over one order of magnitude in aperture (Figure 2).

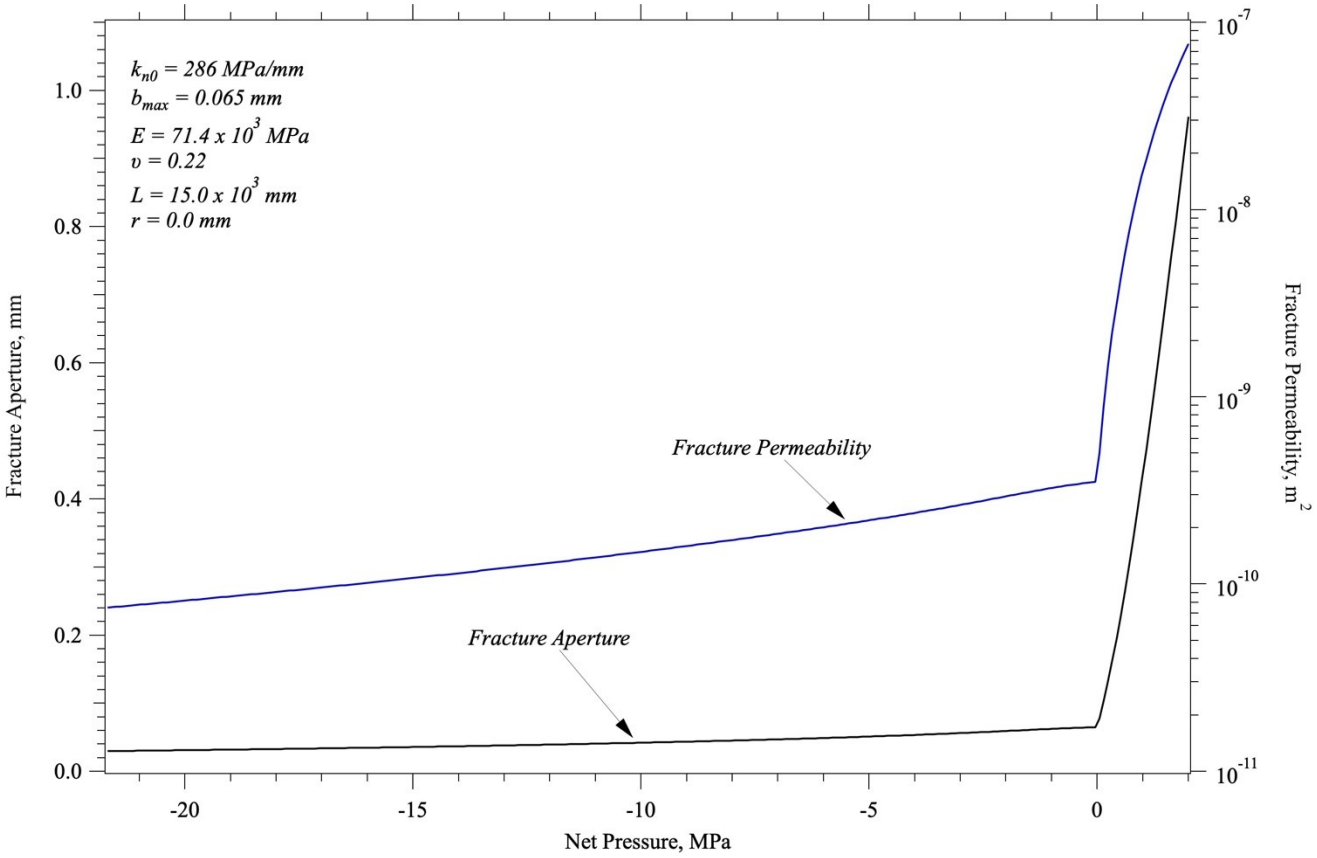

Figure 2: Local fracture aperture model, spanning negative and positive net pressure.

An assessment of the appropriateness of the described fracture aperture model was made by comparing fracture aperture computed by GEOS (Settgast *et al.*, 2017) at the completion of hydraulic fracture propagation simulation for the Experiment 1 testbed under a thermally altered stress state with a stochastically generated stress variation. The fracture circumferential geometry was used to develop triangulated discretization of the fracture, and then a distribution of overall radii and distances from the local fracture centroid were computed for each fracture triangle centroid. Fracture pressure and normal stress from the GEOS simulation were interpolated onto the discretized fracture, and a fracture aperture was computed for each fracture triangle. For these calculations $b_{max} = 0.065\ mm$, $k_{no} = 286\ MPa/mm$, $E = 71.4\ x\ 10^3\ MPa$, and $\nu = 0.22$, and the distribution of normal stress interpolated onto the discretized triangle surface is shown in Figure 3. Only a small portion of the fracture, near the lower fringes, was under negative net pressure conditions, therefore, this comparison is generally for the open aperture component of the model. The apertures from the described model in Figure 4(b), compare reasonably well with those from the GEOS computed aperture in Figure 4(a), both in absolute values and distribution. The GEOS computed apertures

have more structure which is reflective of the stress distribution (Figure 3) than the described model, but otherwise the aperture distributions are comparable. This comparison is limited to a single isolated hydraulic fracture, making the model assumptions appropriate. For more complex fracture networks, stress shadowing could yield poorer comparisons between the more comprehensive GEOS computed apertures and the local fracture aperture model.

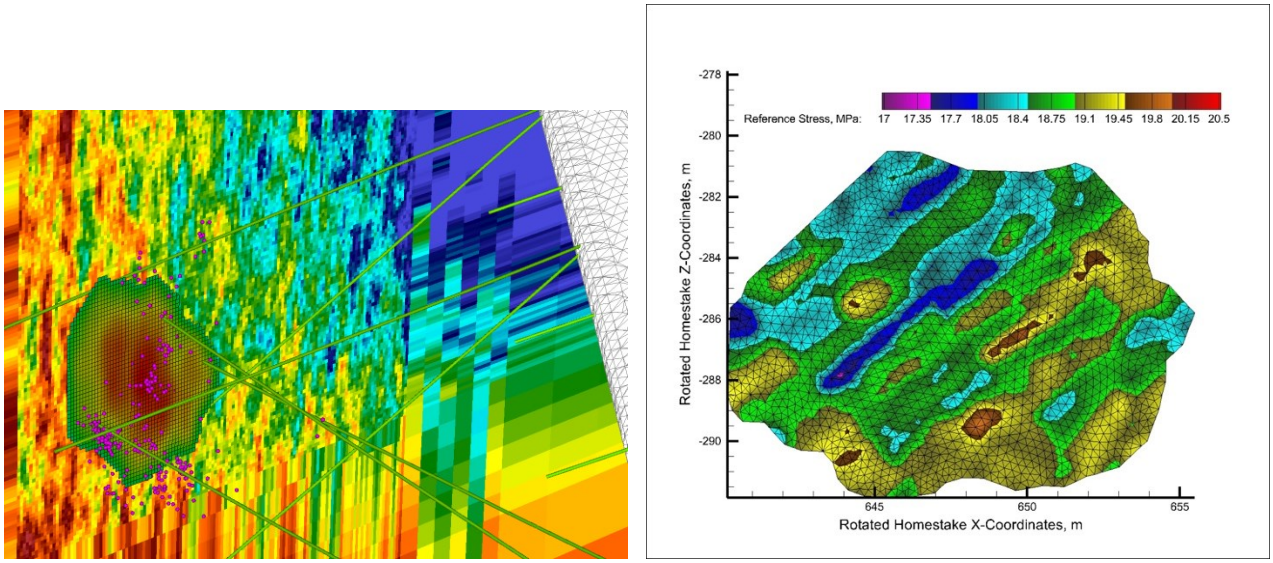

Figure 3: (a) GEOS simulation of fracture propagation, including rock property and stress heterogeneity, and (b) normal stress from GEOS simulation interpolated onto the discretized fracture (image flipped vertically from in-situ image).

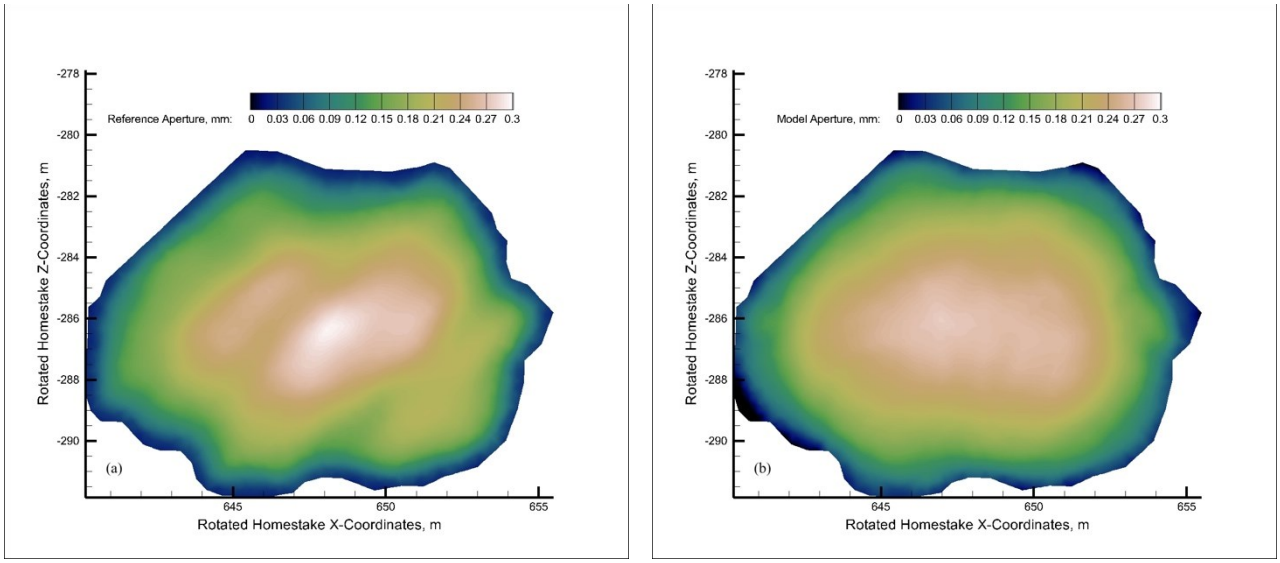

Figure 4: (a) Fracture aperture computed by GEOS, and (b) fracture aperture computed via the local fracture aperture model.

3. NUMERICAL MODEL

The principal objective of this simulation study is to investigate whether the experimental observation of increasing flow resistance over time, as shown in Figure 1, for the long-term chilled-water circulation test could be the consequence of increased stress on the hydraulic fracture from leaked off water. The described fracture aperture model provides a scheme for computing the aperture of the hydraulic fracture in response to changes in the net pressure distribution. A series of simulations were executed with the STOMP-GT simulator with the described fracture aperture model. A Cartesian computational domain of 31 x 51 x 41, having a uniform spacing of 1.25 m was generated and then aligned with the principal geomechanical stress directions. The hydraulic fracture generated from the E1-I borehole from the notch at 50 m (164 ft) from the collar was discretized as planar circle with a radius of 10 m, in agreement with seismic event locations during the stimulation stages. The OT-P connector natural fracture was discretized as a planar circle with a radius of 15 m, in agreement with core logs from E1-OT and E1-P. Both the hydraulic and OT-P natural fractures were modeled as embedded features in the rock matrix domain (White *et al.*, 2020) providing hydraulic and thermal communication between the fracture and rock matrix and across fractures. The rock matrix was initialized using the temperature distribution computed by considering the historical cooling,

flooding and subsequent reopening of the West Access Drift on the 4850 Level (White *et al.*, 2019). The rock matrix was considered to be in hydrostatic equilibrium with a nominal initial pressure of 8.3 MPa. Both fractures were initialized under hydrostatic conditions with a nominal pressure of 20 MPa at 20˚C. Petrophysical properties of the rock matrix (i.e., phyllite) and other parameters used in the simulations are listed in Table 1. The initial fracture pressure and minimum horizontal stress (σ_v) yield negative initial net pressures within the hydraulic fracture. The rock matrix computational mesh, discretized fractures, initial temperature distribution, initial fracture apertures, West Access drift location, and borehole trajectories are shown in Figure 5.

Table 1. Experiment 1 Testbed Phyllite Petrophysical Properties

Property	Value	Property	Value	Property	Value
Grain Density	2900 kg/m^3	Thermal Conductivity	5.0 W/m K	Residual Saturation	0.06
Porosity	0.01	van Genuchten α	0.186 1/m	σ_h	21.7 MPa
Pore Compressibility	7.2 x 10^{-16} 1/Pa	van Genuchten n	1.529	σ_H	35.5 MPa
Grain Specific Heat	805 J/kg K	van Genuchten m	0.346	σ_V	41.8 MPa

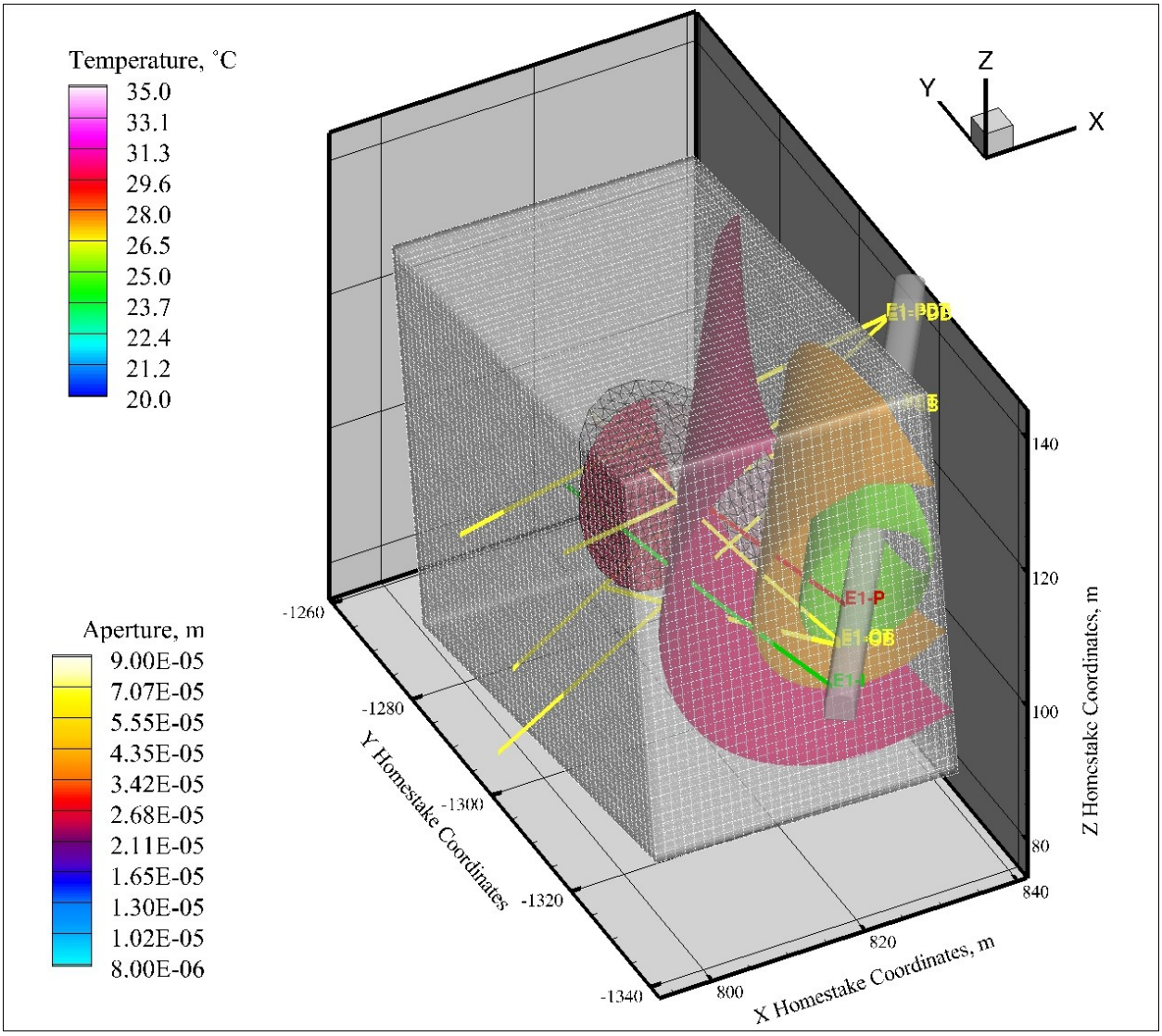

Figure 5: Rock matrix computational grid, embedded fracture grids, initial temperature iso-surfaces, initial fracture aperture, and location of the West Access drift, for b_{max} = 0.0323 mm.

Boreholes were modeled using an embedded approach (White *et al.*, 2020). The E1-I borehole was modeled via two borehole elements, a short section of borehole that spanned the hydraulic fraction near the notch at 50 m (164 ft), similar to the packed interval of the experimental borehole. A constant flow rate (0.4 L/min), constant temperature (11 ˚C) boundary condition was applied to this borehole. A skin factor (i.e., flow resistance) was applied between this borehole interval and the hydraulic fracture. A second section of borehole from the collar to the top of the packed interval was modeled as a constant temperature borehole. This borehole section was designed to model the impact of the injection water cooling system used in E1-I, which comprised a concurrent tube-in-tube heat exchanger design. For this borehole, the borehole casing was maintained at 11 ˚C. The below interval and interval sections of the E1-P borehole were modeled with two short sections of borehole nodes. Constant pressure conditions were imposed on the boundaries of these sections of borehole nodes. It should be noted that the E1-P borehole was open to atmospheric conditions at the collar, so the pressure imposed on these boundaries assumed a hydrostatic gradient from the borehole collar to the borehole section (i.e., 0.1868 MPa for below the interval, E1-PB, and 0.1817 MPa for the interval, E1-PI). Skin factors were applied between the borehole and connection with a fracture. The below interval section, intersected the hydraulic fracture, and the OT-P connector natural fracture intersected the interval section. The fracture aperture model permits the hydraulic fracture to have portions of the fracture under opening and closure conditions concurrently. For example, in the early stages of a simulation with a b_{max} = 0.025 mm, which would ultimately result in E1-I borehole pressures above those observed during the long-term chilled-water circulation test, the region around injection borehole was under opening conditions, whereas the remainder of the fracture was under closure conditions, as shown in Figure 6.

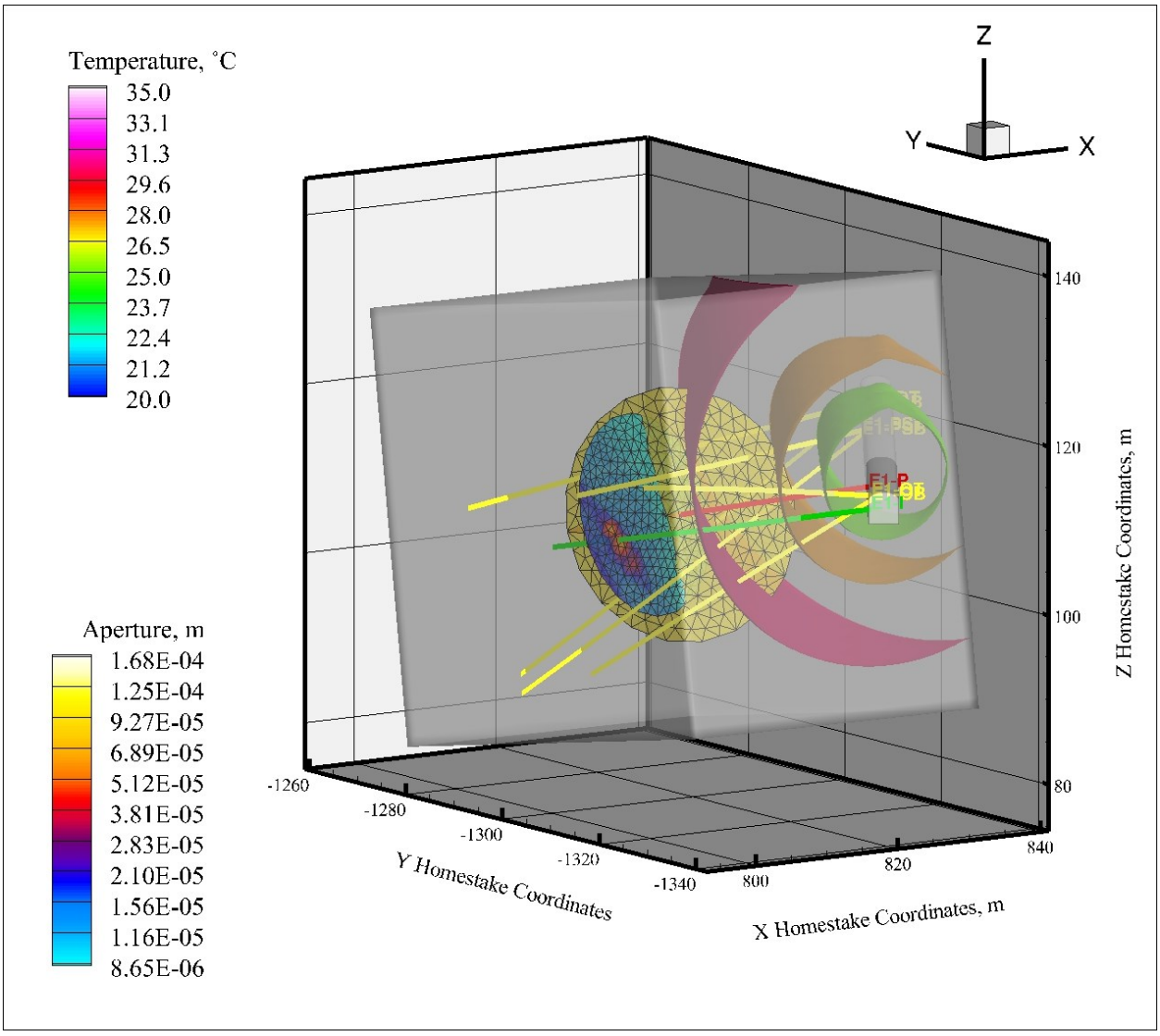

Figure 6: Aperture variation across the hydraulic fracture during the early stages of injection with a b_{max} = 0.025 mm, showing opening conditions around E1-I and closure conditions elsewhere. The OT-P connector natural fracture was maintained at 0.096 mm.

4. SIMULATION RESULTS

Simulations were executed on all three grid systems simultaneously in one implicit nonlinear system solve. Three conservation equations (water mass, air mass, and energy) were solved at each rock matrix grid cell, fracture triangle volume, and borehole node, yielding a system of 198,315 coupled equations. The conservation of air mass equation is not required for these simulations, but is included in STOMP-GT, as it is designed to solve multiphase problems. The simulation period in all simulations was 196 days, the length of the long-term, chilled-water circulation test. The experimental benchmark for these simulations was the record of E1-I pressure, shown in Figure 1. As the production borehole interval pressures were maintained at constant pressure conditions, the E1-I pressure served as an indicator of flow resistance (i.e., the greater the injection interval pressure, the greater the flow resistance).

The long-term chilled-water circulation test is defined by a pressure drop of roughly 33.8 MPa between E1-I and E1-P. For simulation purposes that pressure drop occurs at the E1-I to hydraulic fracture intersection via the S_I skin factor, via flow resistance across the hydraulic and natural OT-P connector fractures, at the E1-PB to hydraulic intersection via the S_{PB} skin factor, and at the E1-PI to OT-P connector fracture via the S_{PI} skin factor. The flow resistance across the hydraulic fracture is determined via the fracture aperture, which varies spatially and temporally, according to the described fracture aperture model. A key parameter in this model is the fracture aperture at zero net pressure. Using skin factors determined from previous fixed aperture conditions (White *et al.*, 2020) two simulations were executed that differed only in the fracture aperture at zero net pressure: 1) b_{max} = 0.055 mm and 2) b_{max} = 0.035 mm. Although EGS reservoirs are nominally considered to be impermeable, the large surface areas and high pressure differentials between the fracture fluid and matrix pore fluid due yield leakoff of fluids between the fracture and rock matrix. For the long-term chilled-water circulation test, the initial matrix pore pressure was estimated at 8 MPa, which is above the E1-P pressures, but below the E1-I pressures. During the development of the Experiment 1 testbed, water drained from E1-P for a period of time after drilling, presumably from the OT-P connector fracture. This would suggest a lower initial pore pressure could be justified for the matrix near the OT-P connector fracture, but a uniform pressure of 8.3 MPa was applied, assuming hydrostatic conditions.

In the simulation, shown in Figure 7, with a b_{max} = 0.055 mm, the fracture pressures remain below 8.3 MPa, resulting in negative leakoff (i.e., flow from the matrix to the fracture), controlled by the fracture-matrix pressure differential and matrix permeability of $k = 1 \times 10^{-19}$ m^2, as shown in Figure 9. Both the global and local fracture leakoff rates are negative throughout the simulation, except for near the injection interval, and most of the transient decay in leakoff rate occurs within a few days. Global fracture and local fracture leakoff rates for the simulation shown in Figure 8, with a b_{max} = 0.035 mm, are shown in Figure 10. Because of the additional flow resistance across the hydraulic fracture, leakoff direction varies across the fracture, being positive near the fluid injection point at E1-I and negative near the fluid production point at E1-PB. Regardless of the leakoff direction, the transient leakoff rate occurs over the first couple of days, again controlled by the fracture-matrix pressure differential and matrix permeability of $k = 1 \times 10^{-19}$ m^2. Experimental measurements (Frash *et al.*, 2019) of matrix permeability of samples prepared from cores taken during the drilling of the boreholes within the Experiment 1 testbed indicated values less than 0.001 mD or roughly 1×10^{-18} m^2, with the permeability of the sealed natural fractures being equivalent. Numerical simulations of evaporation rates from the drift walls (White *et al.*, 2019) yielded matrix permeabilities of 0.005 mD or roughly 5×10^{-18} m^2 for near-surface rock.

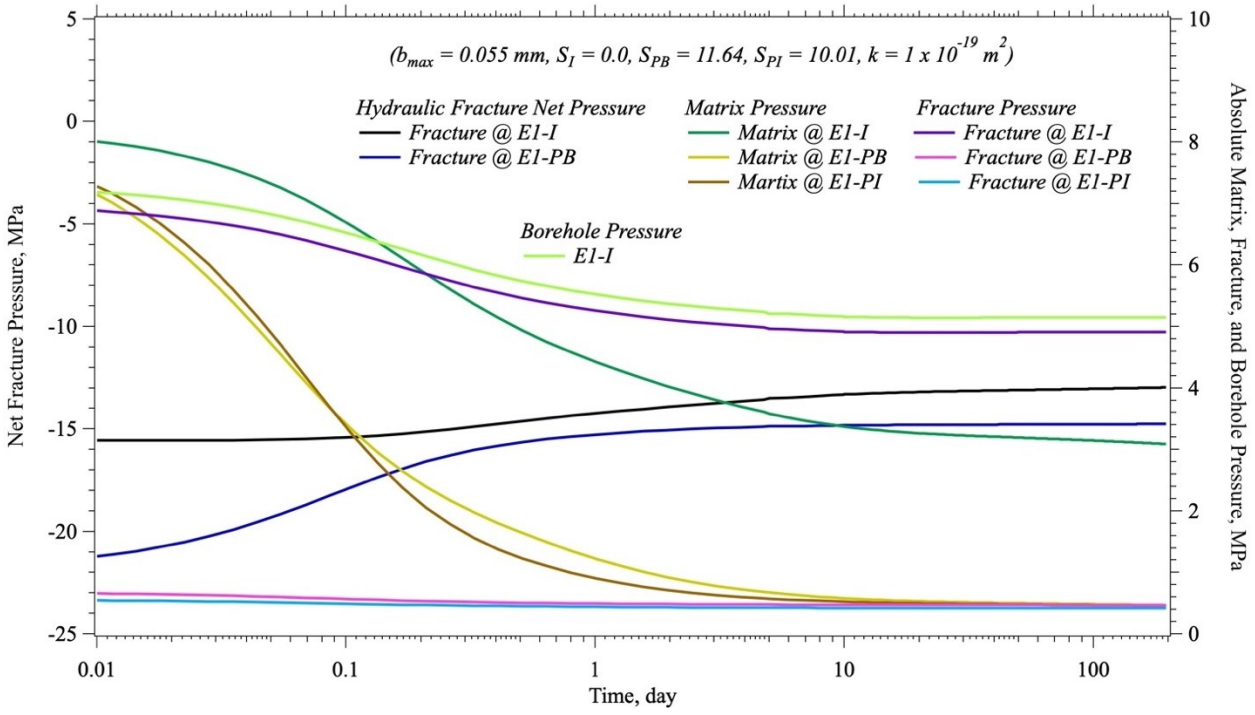

Figure 7: Hydraulic fracture net pressure, matrix absolute pressure, fracture absolute pressure, and borehole pressure versus time at boreholes E1-I and E1-P for b_{max} = 0.055 mm, S_I = 0.0, S_{PB} = 11.64, S_{PI} = 10.01, k = 1 x 10^{-19} m^2.

Plots of net pressure within the hydraulic fracture and absolute pressure in the matrix, fracture and borehole are shown in Figure 7, for locations near the E1-I and E1-P boreholes, for b_{max} = 0.055 mm. For these parameters the hydraulic fracture remains in the closure regime, but the zero net pressure aperture was sufficiently large to keep the flow resistance to minimal values, even with the relatively high skin factors. The resulting E1-I borehole pressure was slightly above 5 MPa, significantly below the experimental values approaching 33.8 MPa at the end of the test. Reducing the zero net pressure aperture to 0.035 mm increases the flow resistance across the network (Figure 8), with a peak E1-I borehole pressure slightly above 26 MPa, a five-fold increase in flow resistance across the fracture network for a 0.02 mm reduction in the fracture aperture at zero net pressure, indicating the sensitivity of this parameter. Unlike the simulations using fixed fracture apertures (White *et al.*, 2020), skin factors were not required at the E1-I borehole-fracture connection.

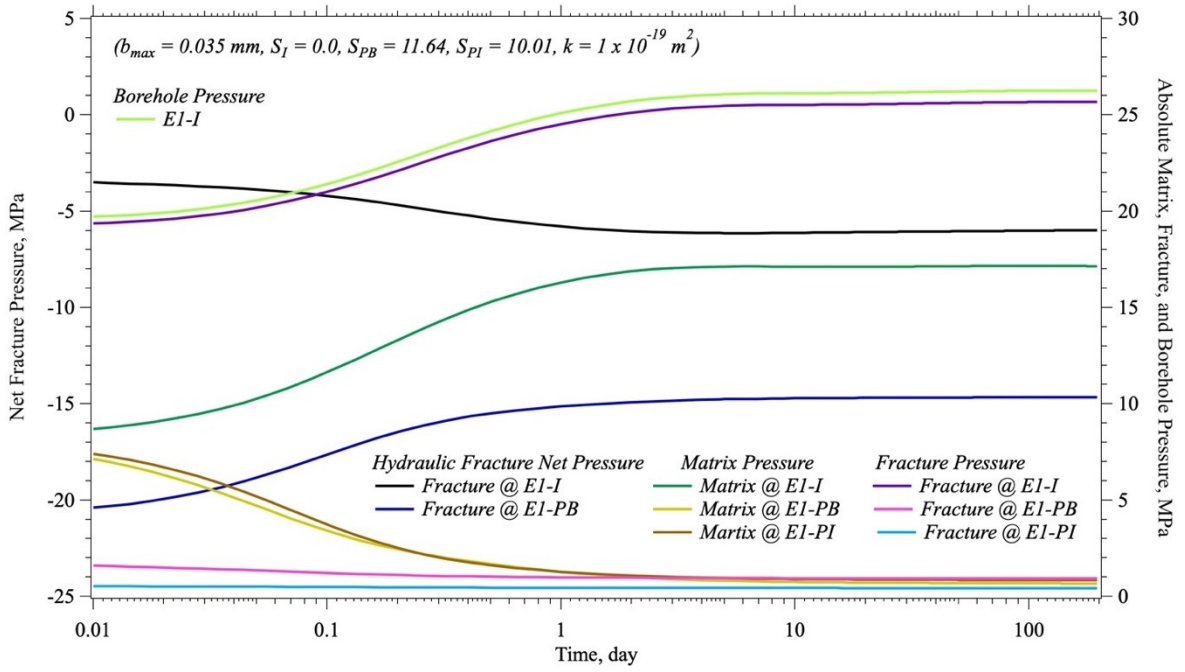

Figure 8: Hydraulic fracture net pressure, matrix absolute pressure, fracture absolute pressure, and borehole pressure versus time at boreholes E1-I and E1-P for b_{max} = 0.035 mm, S_I = 0.0, S_{PB} = 11.64, S_{PI} = 10.01, k = 1 x 10^{-19} m^2.

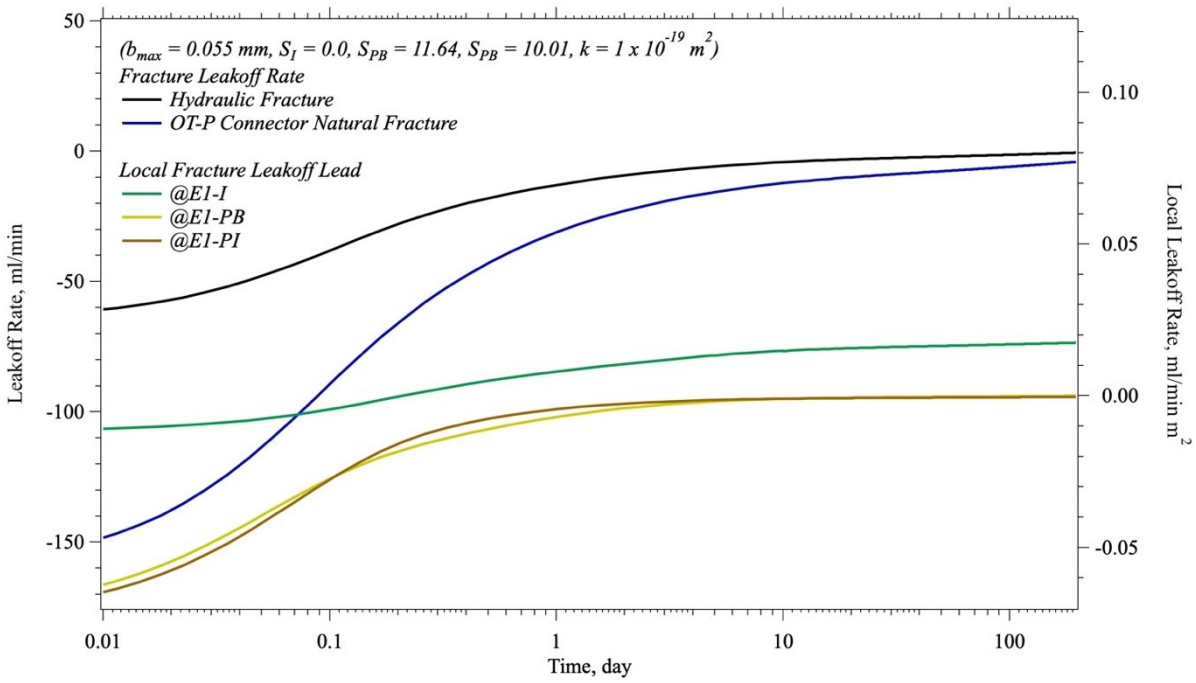

Figure 9: Fracture leakoff rate versus time and local fracture leakoff rate near E1-I, E1-PB, and E1-PI, for b_{max} = 0.055 mm, S_I = 0.0, S_{PB} = 11.64, S_{PI} = 10.01, k = 1 x 10^{-19} m^2.

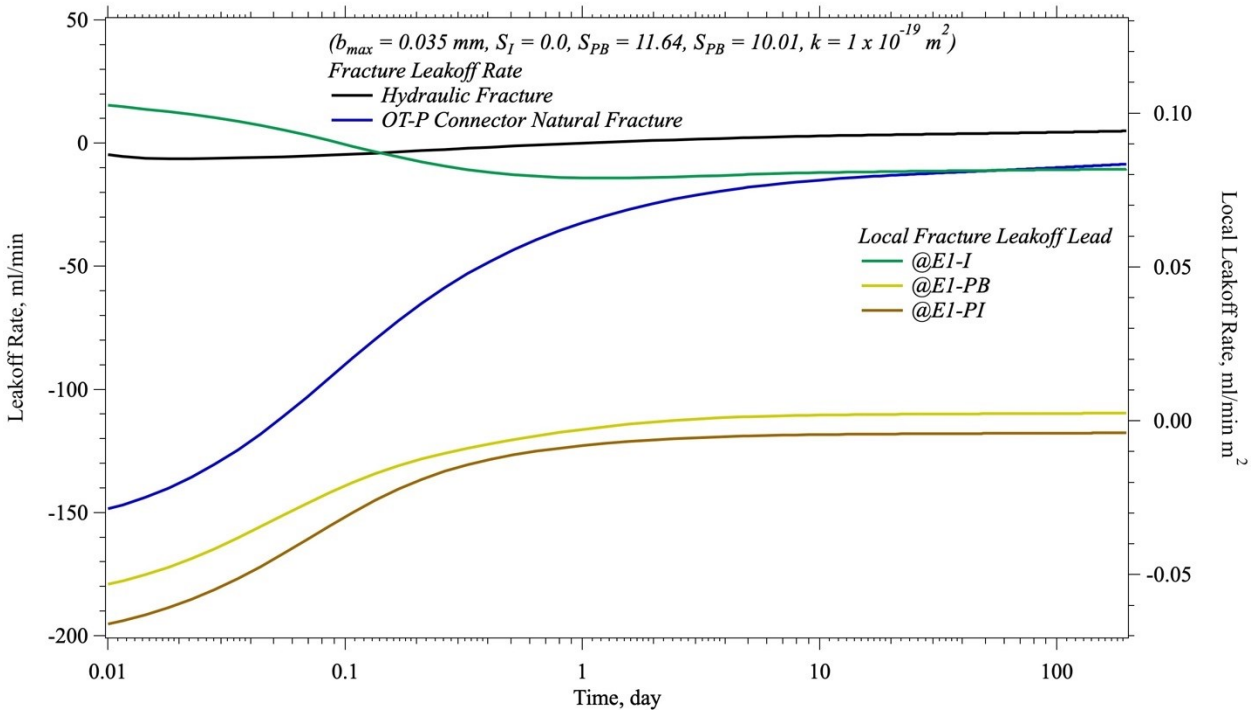

Figure 10: Fracture leakoff rate versus time and local fracture leakoff rate near E1-I, E1-PB, and E1-PI, for b_{max} = 0.035 mm, S_I = 0.0, S_{PB} = 11.64, S_{PI} = 10.01, k = 1 x 10^{-19} m^2.

Although EGS reservoirs are nominally considered to be impermeable, the large surface areas and high pressure differentials between the fracture fluid and matrix pore fluid due yield leakoff of fluids between the fracture and rock matrix. For the long-term chilled-water circulation test, the initial matrix pore pressure was estimated at 8 MPa, which is above the E1-P pressures, but below the E1-I pressures. During the development of the Experiment 1 testbed, water drained from E1-P for a period of time after drilling, presumably from the OT-P connector fracture. This would suggest a lower initial pore pressure could be justified for the matrix near the OT-P connector fracture, but a uniform pressure of 8.3 MPa was applied, assuming hydrostatic conditions. In the simulation, shown in Figure 7, with a b_{max} = 0.065 mm, the fracture pressures remain below 8.3 MPa, resulting in negative leakoff (i.e., flow from the matrix to the fracture), controlled by the fracture-matrix pressure differential and matrix permeability of k = 1 x 10^{-19} m^2, as shown in Figure 8. Both the global and local fracture leakoff rates are negative throughout the simulation, and most of the transient decay in leakoff rate occurs within a few days. Global fracture and local fracture leakoff rates for the simulation shown in Figure 7, with a b_{max} = 0.035 mm, are shown in Figure 9. Because of the additional flow resistance across the hydraulic fracture, leakoff direction varies across the fracture, being positive near the fluid injection point at E1-I and negative near the fluid production point at E1-PB. Regardless of the leakoff direction, the transient leakoff rate occurs over the first couple of days, again controlled by the fracture-matrix pressure differential and matrix permeability of k = 1 x 10^{-19} m^2. Experimental measurements (Frash *et al.*, 2019) of matrix permeability of samples prepared from cores taken during the drilling of the boreholes within the Experiment 1 testbed indicated values less than 0.001 mD or roughly 1 x 10^{-18} m^2, with the permeability of the sealed natural fractures being equivalent. Numerical simulations of evaporation rates from the drift walls (White *et al.*, 2019) yielded matrix permeabilities of 0.005 mD or roughly 5 x 10^{-18} m^2 for near-surface rock.

For simulation shown in Figures 7 and 9, the hydraulic fracture transitions from having positive leakoff (i.e., flow from fracture to matrix) near the injection borehole, and negative leakoff (i.e., from matrix to fracture). The OT-P connector natural fracture is only under negative leakoff conditions. In addition the entire hydraulic fracture is under negative net pressures, indicating the fracture is under a closure state, with the Bandis fracture aperture model (Bandis *et al.*, 1983) dominating. The combination of net pressure and fractional radial distance was used to determine the local fracture aperture. A formal parameter estimation scheme was not applied to determine values for the fracture aperture at net zero pressure and the skin factors, but using b_{max}=0.0323 mm, S_I = 0.0, S_{PB} = 11.64, S_{PI} = 10.01, yielded a reasonable agreement with the experimental results in terms of flow resistance. One note of exception is that the rise in injection pressure over time occurred within the first two days, versus the experimental observation of the pressure rising over the course of the test. Simulation results in terms of the temperature profile within the rock matrix and the aperture distribution within the hydraulic fracture for these parameters at 196 days (i.e., the end of the long-term chilled-water circulation test) are shown in Figure 11. Higher fracture apertures occur near the center of the fracture and toward the injection borehole, compared with regions near the fracture perimeter and production borehole. Also shown in Figure 10 is the temperature distribution within the testbed, via iso-surfaces of temperature at 25, 27.5, and 30˚C. Whereas some cooling of the rock occurs from the circulation of chilled water across the fracture network, the tube-in-tube chiller system within the E1-I borehole, had a greater impact on the resulting temperature distribution, as shown in Figure 11. The large surface areas of the hydraulic and OT-P connector fractures and low flow rate of the test, yielded only slight cooling of the adjacent rock mass, with the production water arriving at a near equilibrium temperature with the rock, as also noted for the constant aperture simulations(White *et al.*, 2020).

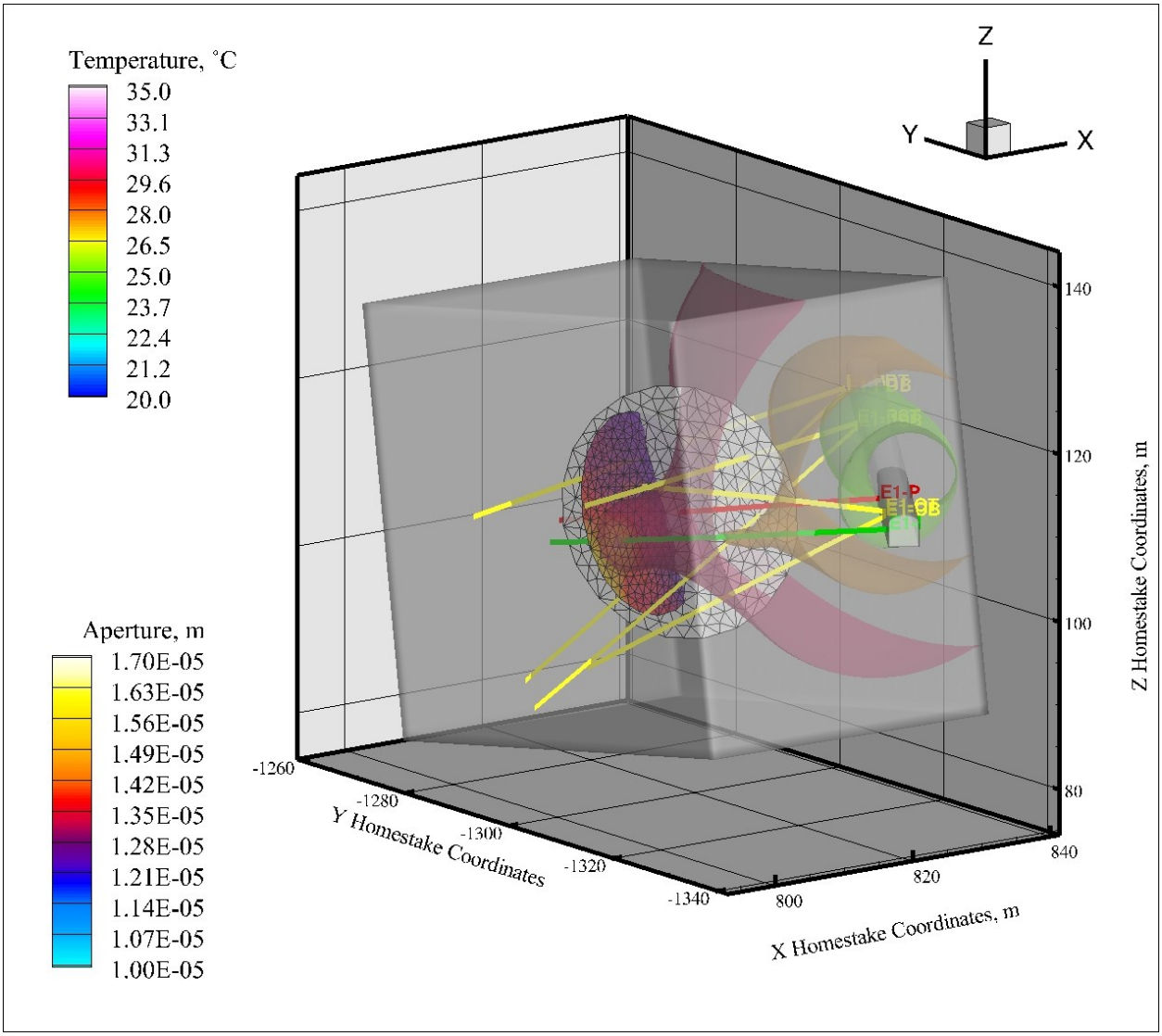

Figure 11: Rock matrix computational domain (shown without mesh), embedded fracture grids, temperature iso-surfaces, fracture aperture, and location of the West Access drift, for b_{max} = 0.0323 mm at 196 days.

The long-term, chilled-water circulation tests differs from field-scale EGS in terms of its length scale, but also because of the low pressures in the production borehole intervals. With fluid injection pressures ranging between 29 and 34 MPa over the course of the test and production pressures at roughly 0.18 MPa, there is a substantial pressure drop across the fracture network. With the matrix pore pressure estimated at 8.3 MPa, a fraction of the fracture network is under positive pressure with respect to the matrix, but another portion of the fracture is under negative pressure. Pressure drops occur at borehole-fracture intersections, fracture-fracture intersections, and across fractures. Skin factors were used to model borehole-fracture intersections, with values for the intersections of the OT-P natural fracture and hydraulic fracture with the E1-P borehole determined from numerical simulations with static fracture apertures (White *et al.*, 2020). Flow resistance across the fracture network of the long-term chilled-water circulation test for fracture closure conditions was most sensitive to the hydraulic fracture aperture at zero net pressure. To investigate the impact of leakoff rate on fracture normal stress and fracture aperture, as series of three simulations were executed with four different matrix permeabilities (i.e., k = 1 x 10^{-18}, 1 x 10^{-19}, 1 x 10^{-20}, 1 x 10^{-21} m^2), maintaining other flow resistance parameters constant (i.e., b_{max}=0.0323 mm, with S_I = 0.0, S_{PB} = 11.64, S_{PI} = 10.01). Results in terms of leakoff rate and timing, and flow resistance across the fracture network are shown in Figure 12. Matrix permeabilities of k = 1 x 10^{-20} m^2 and k = 1 x 10^{-21} m^2 yield increases in the injection pressure that bound the experimental observations (Figure 12). Whereas this result might suggest the gradual rise in injection pressure over time in the experiment could be explained via poroelastic effects due to slow leakoff rates (i.e., low matrix permeabilities), the permeability values needed to achieve this result are not in agreement with the experimentally measured values of k = 1 x 10^{-18} m^2 (Frash *et al.*, 2019). As the pressure in the OT-P connector remained low, through its connection with the production borehole within the packer interval (i.e., E1-PI), increased normal stress on the hydraulic fracture did not occur through inflation of the OT-P natural fracture.

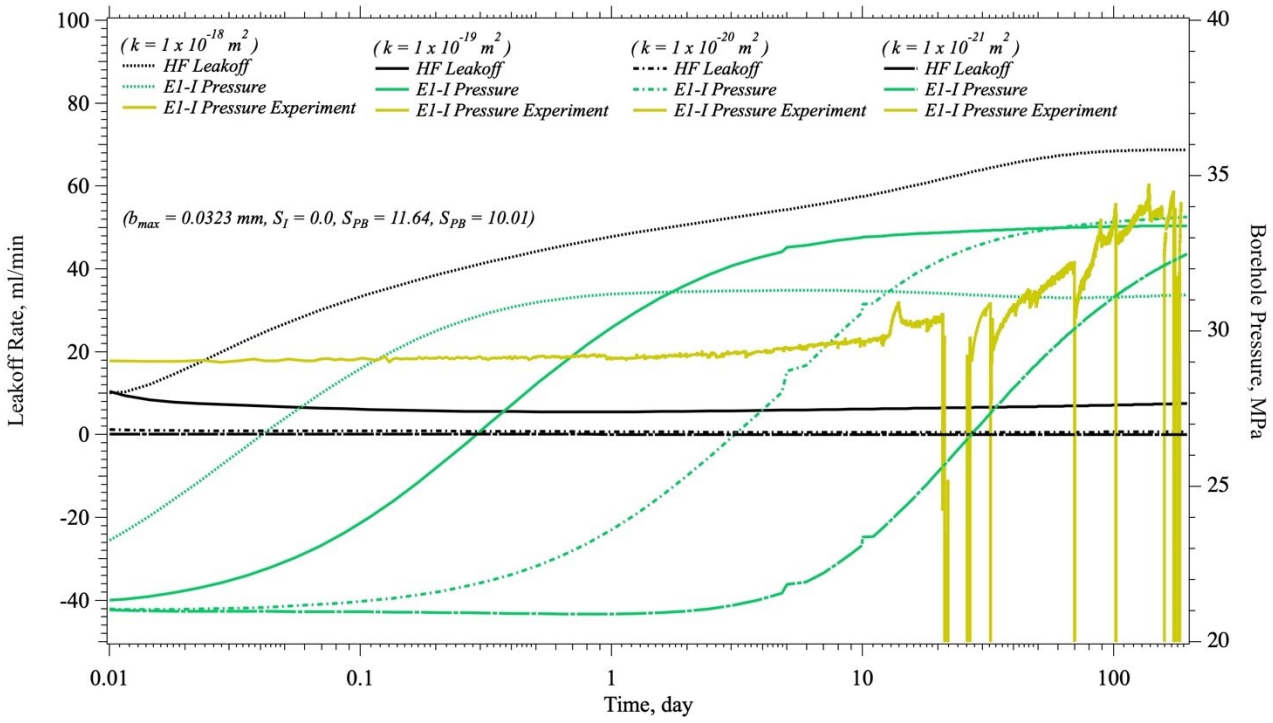

Figure 12: Impact of matrix permeability on leakoff rate, leakoff timing, and flow resistance across the fracture network and comparison of simulation against experimental results, with time zero for the experiment being the start of chilled water injection.

5. CONCLUSIONS

An embedded fracture and borehole modeling approach with a local fracture aperture model was applied to the long-term chilled-water circulation test that was conducted with the Experiment 1 testbed of EGS Collab, a U.S. DOE, Office of Energy Efficiency and Renewable Energy, Geothermal Technologies Office funded project. The local fracture aperture model joined the Bandis fracture closure model with the Sneddon fracture opening model into a continuous function between net fracture pressure and fracture aperture. This model ignores the impact of shear stress, remote changes in fracture aperture on local fracture aperture, and assumed a fixed fracture extent. Whereas the model does not have general applicability, it provided a tool for investigating the dynamic nature of the hydraulic fracture of the long-term, chilled-water circulation test. Simulation results in terms of the flow resistance across the fracture network were found to be most sensitive to the fracture aperture at zero net pressure (b_{max}), with a value of 0.032 mm yielding agreement with the experimental observations. Low b_{max} values yielded high flow resistances and injection pressures, and variable fracture aperture conditions across the hydraulic fracture, with opening conditions near the injection borehole, and closure conditions toward the production borehole. At a value of b_{max} = 0.032 mm, the entire hydraulic fracture was under closure conditions. It remains uncertain what effect a non-locally coupled fracture aperture model would have on these results. The objective of this numerical study was to understand whether increased poroelastic stress on the hydraulic fracture from leakoff could explain the gradual rise in flow resistance or injection pressure over the course of the test. By varying the matrix permeability, it was possible to generate simulation results with gradually increasing injection pressures, as observed in the experiment. But the matrix permeabilities require to generate this response were not in agreement with measured permeabilities of the host phyllite rock. Using measured matrix permeabilities in the simulations, does yield increases in normal stress on the hydraulic fracture from leakoff, but these effects diminish after a few days, following the classical Carter leakoff model, where leakoff rates are an inverse function of the square root of time the fracture is exposed to pressurized water. The results from these simulations, which do not consider the full complexities of the poroelastic mechanics, suggest that something other than increased poroelastic stress is causing the gradual increase in injection pressure over time. As mineral fines were observed in the production fluids throughout the test, clogging remains a mechanism which could explain the injection pressure history of the long-term chilled-water circulation test.

ACKNOWLEDGEMENTS

This material was based upon work supported by the U.S. Department of Energy, Office of Energy Efficiency and Renewable Energy (EERE), Office of Technology Development, Geothermal Technologies Office, under Award Number DE-AC05-76RL01830 with PNNL. The United States Government retains, and the publisher, by accepting the article for publication, acknowledges that the United States Government retains a non-exclusive, paid-up, irrevocable, world-wide license to publish or reproduce the published form of this manuscript, or allow others to do so, for United States Government purposes. We thank the drillers of Agapito Associates, Inc., for their skill and dedicated efforts to create our test bed boreholes. The research supporting this work took place in whole or in part at the Sanford Underground Research Facility in Lead, South Dakota. The assistance of the Sanford Underground Research Facility and its personnel in providing physical access and general logistical and technical support is gratefully acknowledged.

REFERENCES

Bandis, S. C., Lumsden, A. C. & Barton, N. R. (1983). *Int J Rock Mech Min* **20**, 249-268.

Dobson, P. F., Kneafsey, T., Blankenship, D., Valladao, C. A., Morris, J. P., Knox, H., Schwering, P., White, M. D., Doe, T., Roggenthen, W., Mattson, E., Podgorney, R., Johnson, T. C., Ajo-Franklin, J. & Team, E. C. (2017). *Geothermal Resources Council Transactions* **41**, 837-849.

Dobson, P. F., Kneafsey, T. J., Blankenship, D., Morris, J. P., Fu, P., Knox, H., Schwering, P., Ingraham, M., White, M. D., Johnson, T., Burghardt, J. A., Doe, T., Roggenthen, W., Neupane, G., Podgorney, R., Horne, R. N., Hawkins, A., Singh, A., Huang, L., Frash, L. P., Weers, J., Ajo-Franklin, J., Schoenball, M., Ulrich, C., Mattson, E., Uzunlar, N., Valladao, C. A. & Team, E. C. (2020). *World Geothermal Congress 2020*. Reykjavik, Iceland.

Frash, L. P., Carey, J. W., Welch, N. J. & EGS Collab Team, t. (2019). EGS Collab Experiment 1: Geomechanical and Hydrological Properties by Triaxial Direct Shear, 44th Workshop on Geothermal Reservoir Engineering, Stanford University, Stanford, California.

Kneafsey, T., Blankenship, D., Dobson, P. F., Knox, H., Johnson, T. C., Ajo-Franklin, J., Schwering, P., Morris, J. P., White, M. D., Podgorney, R., Roggenthen, W., Doe, T., Mattson, E., Valladao, C. A. & Team, E. C. (2018). *Geothermal Resources Council Transactions* **42**.

Kneafsey, T., Blankenship, D., Dobson, P. F., Morris, J. P., White, M. D., Knox, H., Johnson, T. C., Ajo-Franklin, J., Schwering, P., Fu, P., Podgorney, R., Huang, L., Johnston, B., Roggenthen, W., Doe, T., Mattson, E. & Valladao, C. A. (2019). *Geothermal Resources Council Transactions* **43**, 366-367.

Kneafsey, T. J., Blankenship, D., Dobson, P. F., Morris, J. P., White, M. D., Fu, P., Schwering, P. C., Ajo-Franklin, J. B., Huang, L., Schoenball, M., Johnson, T. C., Knox, H. A., Neupane, G., Weers, J., Horne, R., Zhang, Y., Roggenthen, W., Doe, T., Mattson, E., Valladao, C. & EGS Collab Team, t. (2020). The EGS Collab Project: Learnings from Experiment 1, 45th Workshop on Geothermal Reservoir Engineering, p. 15. Stanford University, Stanford, California.

Moore, J. (2020). The Utah FORGE: An International Laboratory for Advancing Enhanced Geothermal Development, AAPG Explorer.

Moore, J., McLennan, J., Pankow, K., Simmons, S., Podgorney, R., Wannamaker, P., Jones, C., Rickard, W. & Xing, P. (2020). *45th Workshop on Geothermal Reservoir Engineering*. Stanford University, Stanford, California, USA.

Oldenburg, C. M., Dobson, P. F., Wu, Y., Cook, P. J., Kneafsey, T., Nakagawa, S., Ulrich, C., Siler, D. L., Guglielmi, Y., Ajo-Franklin, J., Rutqvist, J., Daley, T. M., Birkholzer, J. T., Wang, H. F., Lord, N. E., Haimson, B. C., Stone, H. L., Vigilante, P., Roggenthen, W. M., Doe, T. W., Lee, M. Y., Ingraham, M., Huang, H., Mattson, E. D., Zhou, J., Johnson, T. J., Zoback, M. D., Morris, J. P., White, J. A., Johnson, P. A., Coblentz, D. D. & Heise, J. (2016). Lawrence Berkeley National Laboratory.

Settgast, R. R., Fu, P. C., Walsh, S. D. C., White, J. A., Annavarapu, C. & Ryerson, F. J. (2017). *Int J Numer Anal Met* **41**, 627-653.

Sneddon, I. N. (1946). *Proc R Soc Lon Ser-A* **187**, 229-260.

White, M. D., Fu, P., McClure, M. W., Danko, G., Elsworth, D., Sonnenthal, E., Kelkar, S. & Podgorney, R. (2018). *Geomechanics and Geophysics for Geo-Energy and Geo-Resources* **4**, 79-117.

White, M. D., Fu, P. & Team, E. C. (2020). *45th Workshop on Geothermal Reservoir Engineering*. Stanford University, Stanford, California: Stanford University.

White, M. D., Johnson, T. C., Kneafsey, T., Blankenship, D., Fu, P., Wu, H., Ghassemi, A., Lu, J., Huang, H., Neupane, G., Oldenburg, C. M., Doughty, C. A., Johnston, B., Winterfeld, P., Pollyea, R., Jayne, R., Hawkins, A., Zhang, Y. & Team, E. C. (2019). *44th Workshop on Geothermal Reservoir Engineering*. Stanford University, Stanford, CA, USA.

Wu, K. & Olson, J. E. (2015). *Int J Fracture* **193**, 191-204.